Nonuniform H distribution in thin-film hydrogenated amorphous Si by small-angle neutron scattering

D. L. Williamson*
Department of Physics, Colorado School of Mines, Golden, Colorado 80401

D. W. M. Marr
Department of Chemical Engineering, Colorado School of Mines, Golden, Colorado 80401

J. Yang, B. Yan, and S. Guha
United Solar Systems Corporation, 1100 W. Maple Road, Troy, Michigan 48084
(Received 26 August 2002; published 27 February 2003)

Small-angle neutron scattering (SANS) is used to search for nonuniform H distributions in hydrogenated amorphous silicon, *a*-Si:H. Thin films about 2-μm-thick grown with and without D substitution for H by plasma-enhanced chemical vapor deposition show both large (>20 nm) and small (<8 nm) heterogeneous features. The absolute SANS intensities, however, are small and place stringent upper limits on the degree of H heterogeneity present. These results do not support a recently proposed two-domain, amorphous/paracrystalline model. The presence of a small amount of microcrystallinity yields much stronger SANS intensities, consistent with H accumulation in grain boundary regions and/or enhanced microvoid formation. A clear correlation of the larger scattering features with film surface roughness is found.

DOI: 10.1103/PhysRevB.67.075314 PACS number(s): 81.05.Gc, 68.55.−a, 61.12.Ex, 68.35.Dv

I. INTRODUCTION

Various techniques suggest the presence of heterogeneity in high quality hydrogenated amorphous silicon, *a*-Si:H, developed for solar cells and other devices. Transmission electron microscopy (TEM) shows nanometer-scale, ordered, crystallinelike regions in an amorphous matrix,[1–3] while nuclear magnetic resonance (NMR) data have been interpreted in terms of clustered and isolated H.[4–7] Based on these results as well as earlier small-angle neutron scattering (SANS) analysis,[8] a two-domain model was recently proposed[6,9,10] to explain the observed light-induced volume expansion of *a*-Si:H.[6,11] The model is one of high-density, crystallinelike (“paracrystalline” [12]) regions, about 1–3 nm in size, imbedded in a low-density amorphous matrix. It includes even lower-density boundary regions surrounding the paracrystalline inclusions. This model implies a highly nonuniform H distribution, with H-free, crystal-like inclusions, separated by H-rich boundary layers from the hydrogenated amorphous matrix. The relative volume fractions of the amorphous and crystallinelike regions depend on the deposition method, with significant differences proposed for plasma-enhanced chemical-vapor deposition (PECVD) compared to hot-wire CVD (HWCVD).[5,10] Here we focus on the prominent commercial method for fabricating solar cells, PECVD, for which the paracrystalline volume fractions proposed are about 10–20 %.

With a total H content in PECVD films of about 10–12 at. %, the two-domain model[9,10] proposes levels near 0 at. % in the crystalline-like regions, somewhat lower than 10–12 at. % in the amorphous matrix, and much higher than this in the boundary regions. Due to the significant H scattering cross section and the large difference in scattering between H and D, SANS experiments with hydrogenated and deuterated films allow for a direct test of such a model and provide evidence for alternate morphologies. For these reasons, previous SANS studies have been attempted but either did not detect sufficient signal from device-quality films[13] or investigated materials whose electronic quality was not well defined.[14–16] By working with stacks of a large number of device-quality, relatively thin films, coupled with other signal-enhancing experimental features described below, we overcome issues associated with previous investigations. Using our approach, we have recently shown that there is no detectable light-induced change in the SANS from either PECVD or HWCVD device-quality films,[17] in contrast to an earlier study of sputter-deposited material.[15,8,18] We did, however, observe significant differences in the SANS from PECVD and HWCVD material.[17] In this work we provide SANS data from additional PECVD films, and quantify the results in the context of the proposed two-domain model.[9,10] We also identify the importance of surface roughness in an analysis of SANS data from thin film samples. The samples investigated were made under conditions similar to those that have yielded record high efficiency solar cells[19] as well as under less-optimized conditions for comparison.

II. EXPERIMENT

A set of systematic samples was prepared by rf (13.56 MHz) PECVD in pairs using H- and D-containing source gases, as shown in Table I. Each pair (with H or D) was made under nominally identical conditions of gas flows, gas pressures, substrate temperatures, and deposition rates. Slight adjustments in plasma power and H_2/D_2 dilution ratios were used to generate similar deposition rates for the pairs. Most samples were made under conditions of “high dilution” with H_2 or D_2, which yielded the record devices,[19] as well as better light stability[1,3] and improved medium range order.[20]

 ©2003 The American Physical Society

TABLE I. Samples prepared for SANS. Listed are sample identification numbers (I.D.#), preparation source gases and substrate temperatures (T_s), number of layers used for SANS sample (*N*), total thickness of all layers (*t*), H and D concentrations (C_H and C_D) from IR analyses, and the ratio of IR intensities (*R*) as defined in the text. Experimental uncertainties in C_H and C_D are 10% of the values listed, except for C_H for 1D and 2D, which are ±0.5 at. %, and *R* are ±0.02.

Sample I.D.#	Preparation	*N*	*t* (μm)	C_H (at. %)	C_D (at. %)	*R*
1H	SiH_4 + high H_2 dilution, $T_s = 300\,°C$	12	24.2	11	0	0.12
1D	SiD_4 + high D_2 dilution, $T_s = 300\,°C$	12	20.4	~0.5	13	0.25
2H	SiH_4 + no H_2 dilution, $T_s = 300\,°C$	12	24.8	13	0	0.20
2D	SiD_4 + no D_2 dilution, $T_s = 300\,°C$	12	21.0	~0.5	13	0.23
3H	Si_2H_6 + high H_2 dilution, $T_s = 225\,°C$	12	22.6	15	0	0.17
3HD	Si_2H_6 + high D_2 dilution, $T_s = 225\,°C$	9	23.0	8.5	6	0.24
4H	Si_2H_6 + high H_2 dilution, $T_s = 300\,°C$	8	17.2	12.5	0	0.13
4HD	Si_2H_6 + high D_2 dilution, $T_s = 300\,°C$	10	28.9	7.5	5	0.17

Note that two samples were made with a mixture of H and D using disilane diluted in D_2.

To optimize the signal-to-noise ratio in the SANS measurements,[21] special *c*-Si substrates were used with the following specifications: float-zone wafers, $500 \pm 25\ \mu m$ thick, undoped (resistivity $> 1000\ \Omega$ cm), two-side polished with low surface roughness (<0.5-nm rms roughness, confirmed by atomic-force microscopy (AFM) to be about 0.15 nm), and (100) orientation. The wafers were diced into $2.5 \times 2.5\text{-cm}^2$ squares to allow films to be grown with at least 2.4 cm diameter to take advantage of the maximum neutron beam diameter available (2.2 cm). Films were grown to nominal thicknesses of about 2 μm on groups of four substrates in three sequential depositions to generate 12 layers for stacking in the neutron beam. Due to some variation in the thickness from layer to layer and deposition to deposition and the need for accurate sample thickness in the quantitative SANS analyses (as well as the infrared absorption analyses), a method was developed to measure the thickness of each layer. A few films were measured directly by profilometry and these were used to calibrate the x-ray scattering intensity (Cu-K_α radiation) at the center of the first amorphous diffraction peak (27.8° 2θ in the Bragg-Brentano geometry[20]). This x-ray intensity was then measured for all layers of each sample. The total number of layers used for the SANS measurements and the total thicknesses are listed in Table I. Some of the layers were excluded due to partial delamination of the film from the *c*-Si substrates; hence the use of less than 12 layers in some samples. The neutron absorption by the *c*-Si substrates at a thickness of 0.6 cm is less than 2%.

The SANS experiments were carried out on the 30-m beam line NG-3 of the NIST Center for Neutron Research.[22] Data were collected in the $64 \times 64\text{-cm}^2$ area detector over a momentum transfer range from $q = 0.05$ to 3 nm^{-1} [$q = (4\pi/\lambda)\sin\theta$, where 2θ is the scattering angle and λ is the neutron wavelength] using two detector positions (2 and 13 m from the sample). The 2-m position also utilized a 20-cm offset to maximize the *q* range.[22] A wavelength of 0.60 nm was used with a spread of $\Delta\lambda/\lambda = 34\%$ (full width at half maximum) to prevent double Bragg diffraction from the (100)-oriented *c*-Si substrates. This choice of parameters resulted in a high incident neutron flux of approximately $10^6\ \text{cm}^{-2}\,\text{s}^{-1}$. To reduce background scattering, samples were measured in an evacuated chamber. The observed two-dimensional SANS intensities were circularly symmetric for all samples and therefore circularly averaged before conversion into absolute cross sections ($\text{cm}^{-1}\,\text{str}^{-1}$) using standard procedures[22] that included subtracting the incoherent scattering (*q* independent) due to the substrates. The latter was measured with a stack of the *c*-Si substrates of approximately the same thickness as the samples (12 layers) and confirmed to have a magnitude of $10^{-4}\ \text{cm}^{-1}\,\text{str}^{-1}$,[23] thereby showing that no additional scattering was originating from the sample substrates.

One experiment was done to search for any strong anisotropy in the SANS. Sample 4H was mounted at a tilt angle of 44° relative to the neutron beam and remeasured. There was little change in the SANS intensities after normalizing to the effective thickness of $t/\cos 44°$. This tilting technique has been used in small-angle x-ray scattering studies[24] to reveal evidence of strong anisotropic scattering from some samples due to highly oriented features, typically associated with the growth direction of the film.

For four of the deposition conditions shown in Table I, companion depositions were made on a high-purity Al foil for small-angle x-ray scattering (SAXS) measurements. Details of the SAXS system, measurement techniques, and quantitative data interpretation are available elsewhere.[24] Results from these experiments were compared with those from SANS to aid in the interpretation. For example, SAXS will not be sensitive to H/D nonuniformity, while both SAXS and SANS are sensitive to the presence of microvoids.

In order to interpret the role of H and D, their concentrations in each sample were obtained by Fourier transform infrared absorption spectroscopy on one or two layers of a given sample. For the *a*-Si:H films, both the 640-cm^{-1} Si-H bending mode and the 2000-cm^{-1} Si-H stretch modes were used to determine the H content. Calibration factors of 2.3×10^{19} and $1.1 \times 10^{20}\ \text{cm}^{-2}$ were used for these two modes, respectively, based on calibrated samples, in close agreement with earlier calibrations.[25] The Si-D bending mode was shifted to wave numbers too low for measurement; therefore, only the Si-D stretch mode near 1460 cm^{-1} was used to

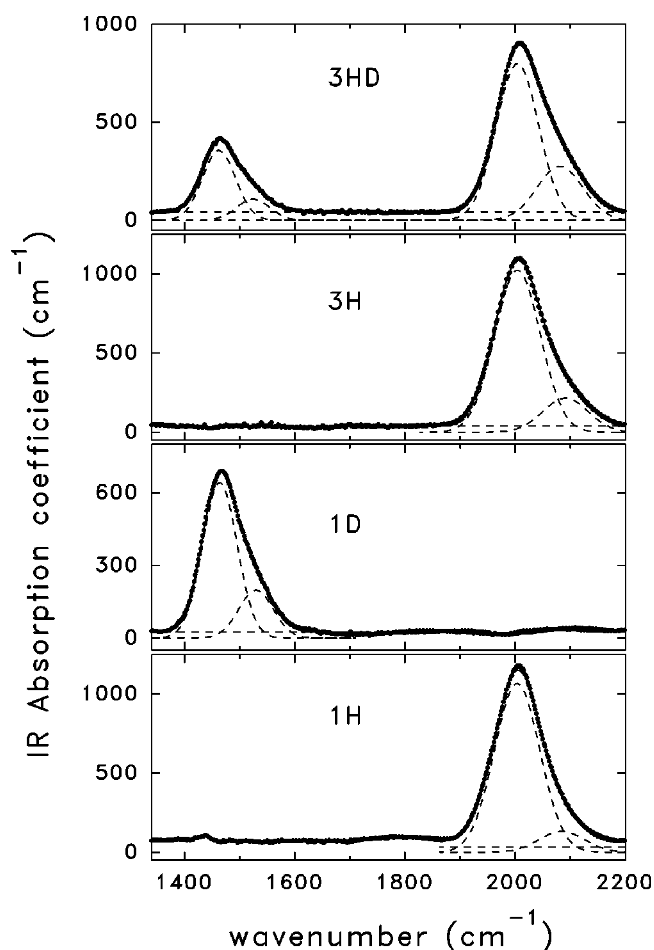

FIG. 1. IR data from four samples as defined in Table I. Two Gaussians and a baseline (dashed lines) are fitted to each mode yielding the solid line passing through the data.

determine the bonded D content. The calibration factor used for this mode was simply $(2)^{1/2}$ that of the Si-H stretch mode based on the masses of H and D.[26] The results of this composition analysis are presented in Table I. For samples 1D and 2D, there was evidence of a small residual H content (~0.5 at. %) due to a weak but nonzero 640-cm^{-1} mode. This is likely due to residual H present in the plasma deposition chamber. Note that significant concentrations of D were introduced from the high D_2 dilution used for samples 3HD and 4HD.

Some structural information is contained in the IR spectra by examining the detailed lineshape of the Si-H and Si-D stretch modes (Fig. 1). Asymmetry in the shape is seen on the high wavenumber side of both modes. This was analyzed by fitting each stretch mode with a superposition of two Gaussians restricted to have the same linewidth and computing the ratio R of the intensity of the higher wavenumber mode (2080–2090 cm^{-1} for H, and 1520–1530 cm^{-1} for D) to the total intensity of both modes. This "microstructure factor" has often been used to characterize the quality of *a*-Si:H, with lower values of R indicating better material since the higher wavenumber mode is associated with more defective material containing Si-H_2 bonds and/or H on internal microvoid surfaces.[27–30] The R values obtained here are

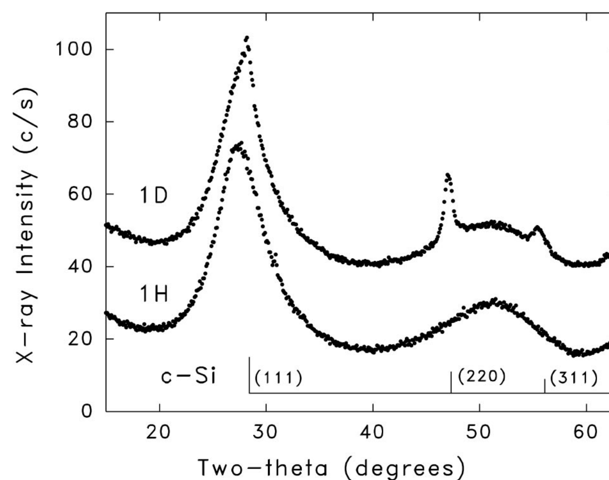

FIG. 2. XRD patterns from two of the SANS samples. The stick diagram shows the relative intensities of the Bragg peaks of the *c*-Si powder pattern.

included in Table I and are low even for the films 2H and 2D prepared without H_2/D_2 dilution, indicating good quality material.[28] For samples 3HD and 4HD, the R's were the same within experimental error (±0.02) for both the Si-H and Si-D modes, indicating the same average local bonding arrangements for the two isotopes.

Surface roughness of two of the samples was characterized by AFM. Sample 1H was relatively smooth and showed a rms vertical roughness of 4.7 nm, with lateral features ranging in size from about 20 nm to more than 100 nm. Sample 1D was significantly rougher, with a vertical rms value of 20 nm and lateral features similar in size to those of 1H. In addition, 1D showed clear circular bubble formation in some regions. These bubbles were of the order of 10 μm in diameter and some had evidently exploded. This is attributed to accumulation of D_2 between the film and *c*-Si substrate during the deposition process. The 20-nm rms roughness of 1D was measured in a region that did not include such bubbles.

To search for evidence of microcrystallinity, x-ray diffraction (XRD) was performed on at least one layer of each sample. These measurements were performed because the deposition condition of high H_2 or D_2 dilution is known to produce films near the onset of microcrystallinity[1] and is dependent on substrate interactions as well as film thickness.[20,31] The XRD measurements were made in the symmetric Bragg-Brentano geometry with Cu-K_α radiation selected by a graphite monochromator in the scattered beam. Figure 2 shows that microcrystallinity was indeed detected in sample 1D. The microcrystalline peaks are shifted to slightly lower angles than those of bulk, powdered *c*-Si (see the stick diagram in Fig. 2), probably due to the typical high compressive stresses in such films. Analysis of the relative areas under the (111), (220), and (311) peaks compared to the areas of the amorphous peaks, as described in Ref. 20, indicates a crystalline volume fraction of about 12% for 1D. Also, the crystallite size is estimated to be about 8 nm based on the width of the XRD peaks and the Scherrer equation.[20] None

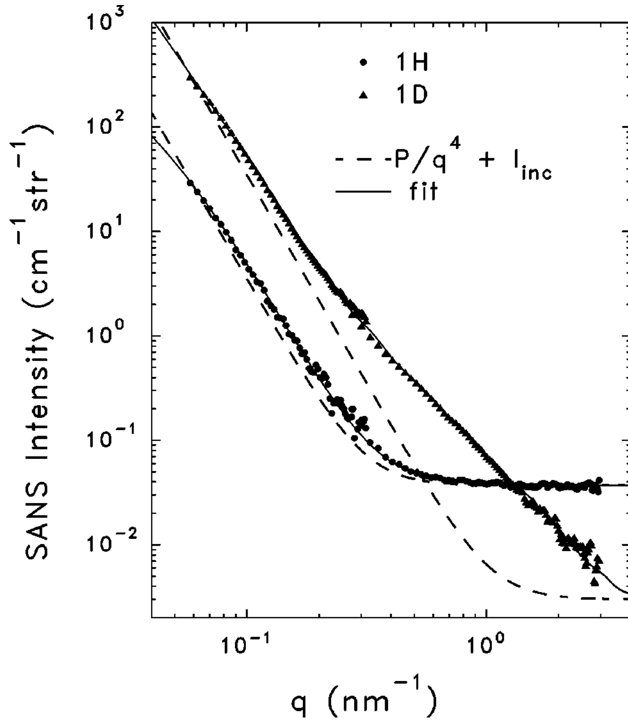

FIG. 3. SANS data from samples 1H and 1D. Solid lines through data are fits of Eq. (7) while the dashed lines show the scattering intensity due only to Porod and incoherent contributions.

of the other samples showed evidence of crystallinity and XRD from the SAXS samples deposited on the Al foil also showed no evidence of crystallinity, even for the 1D companion sample.

III. SANS RESULTS

Figure 3 compares the SANS data from the sample pair 1H and 1D where several features are of interest: (a) the intensities from 1D are much higher than those from 1H over most of the q range; (b) the 1H data at high q reach a well-defined constant level; (c) the 1D data at high q fall well below those from 1H; and (d) both samples show a steep drop in intensity at low q. Features (b) and (c) are readily explained on the basis of the incoherent scattering from H and D. The theoretical expression for this q-independent intensity is

$$I_{\mathrm{inc}}=(n/4\pi)[\sigma_{\mathrm{H}}C_{\mathrm{H}}+\sigma_{\mathrm{D}}C_{\mathrm{D}}], \tag{1}$$

where $\sigma_{\mathrm{H}}=80.26\times10^{-24}\ \mathrm{cm}^2$ and $\sigma_{\mathrm{D}}=2.05\times10^{-24}\ \mathrm{cm}^2$ are the neutron incoherent scattering cross sections[32] of H and D, respectively; C_{H} and C_{D} are the H and D atomic concentrations in the samples, respectively, and n is the average atomic number density of the sample. The incoherent cross section for Si is negligible compared to that of H or D.[32] Taking $n=5.0\times10^{22}\ \mathrm{cm}^{-3}$ and using the concentrations in Table I, one expects $I_{\mathrm{inc}}=0.035\ \mathrm{cm}^{-1}\ \mathrm{str}^{-1}$ for sample 1H, in excellent agreement with the experimental value of $0.037\ \mathrm{cm}^{-1}\ \mathrm{str}^{-1}$ obtained by fitting the data in Fig. 1 at high q. For sample 1D, one expects $I_{\mathrm{inc}}=0.003\ \mathrm{cm}^{-1}\ \mathrm{str}^{-1}$, which is approached, but not reached by the data in Fig. 3. That is, no plateau is found as in the case of 1H. This is apparently due to significant SANS by nanoscale inhomogeneities in this sample causing significant SANS in the high $q=1-3\ \mathrm{nm}^{-1}$ region such that a q-independent region cannot be reached. This level of signal is also approaching the detection limit of the instrument.

The steep drop at low q can be attributed to larger scale objects that can be modeled by the Porod power law intensity[33]

$$I_L=P/q^4, \tag{2}$$

where

$$P=2\pi(\Delta\rho)^2S/V, \tag{3}$$

$\Delta\rho$ is the neutron scattering-length density contrast, and S/V is the total surface area-to-volume ratio of the scattering objects. The dashed lines in Fig. 3 are the sum of Eqs. (1) and (2), illustrating that most of the scattering from sample 1H can be accounted for with these two contributions only, while significant additional scattering is present for sample 1D using the predicted value of $I_{\mathrm{inc}}=0.003\ \mathrm{cm}^{-1}\ \mathrm{str}^{-1}$. The values of P (3.5×10^{-4} and $3.5\times10^{-3}\ \mathrm{cm}^{-1}\ \mathrm{str}^{-1}\ \mathrm{nm}^{-4}$ for 1H and 1D, respectively) cannot yield direct information on the size and volume fraction [as seen by Eq. (3)], but do indicate a larger amount of these larger-scale features of size L in 1D. Since $L\gg1/q$ implies $L\gg10$ nm for the Porod region, and such large features are not expected to be present within the bulk of the films, we propose surface roughness is responsible for this effect. As noted above, AFM measurements were made on these two samples and these data will be useful in supporting this hypothesis.

To model the nanoscale features, a distribution of spherical scattering objects will be used, and to model the surface roughness the Debye correlation-length model[34] will be applied. Specifically, the intensity from a distribution of noninteracting spheres:

$$I_N=A\sum_i w_iR_i^3F^2(qR_i), \tag{4}$$

where A is a constant ($\mathrm{cm}^{-4}\ \mathrm{str}^{-1}$ in absolute cross-section units), R_i is the radius of the ith sphere size, w_i is the relative volume fraction of spheres of size R_i, and $F(qR_i)$ is the scattering form factor for spheres of radius R_i (Ref. 33):

$$F(qR_i)=3[\sin(qR_i)-qR_i\cos(qR_i)]/(qR_i)^3. \tag{5}$$

The correlation-length model intensity (to model the larger sizes, L) is given by[34]

$$I_L=a^3b/(1+a^2q^2)^2, \tag{6}$$

where a is the Debye correlation-length and b is a constant (in absolute cross-section units of $\mathrm{cm}^{-4}\ \mathrm{str}^{-1}$). Note the limiting behavior of q^{-4} at $aq\gg1$ agrees with the Porod law [Eq. (2)].

Thus all of the SANS data are fitted, with the total intensity I_T representing nanoscale and larger scale inhomogeneities, and the incoherent scattering from H and D,

TABLE II. Fit results from SANS analyses. Column labels are defined in text. Uncertainties in the last significant figures are given in parentheses for some quantities. Uncertainties in a and b are approximately 50% and 20%, respectively, of the values shown.

Sample	Q_N (10^{21} cm^{-4})	$\langle d \rangle$ (nm)	a (nm)	b (10^{21} cm^{-4} str^{-1})	Q_L (10^{21} cm^{-4})	I_{inc} (cm^{-1} str^{-1})	I_{inc} (th) (cm^{-1} str^{-1})
1H	0.01(1)	5(3)	30	0.018	0.18(4)	0.037(2)	0.035
1D	2.15(22)	8(1)	50	0.21	2.1(4)	≤0.005	0.003
2H	0.35(4)	4(1)	30	0.004	0.04(1)	0.040(3)	0.042
2D	0.31(3)	4(1)	100	0.012	0.12(3)	≤0.009	0.003
3H	0.23(2)	5(1)	30	0.005	0.05(1)	0.043(3)	0.048
3HD	0.08(1)	5(2)	30	0.004	0.04(1)	0.029(4)	0.028
4H	0.09(1)	7(2)	23	0.011	0.11(2)	0.040(4)	0.040
4HD	0.01(1)	7(3)	40	0.003	0.03(1)	0.023(2)	0.024

$$I_T = I_N + I_L + I_{inc}, \tag{7}$$

where the three contributions are given by Eqs. (1), (4), and (6). The parameters to be adjusted in the fits include the set A, w_i, R_i, a, b, and I_{inc}. The volume-weighted average diameter of the spheres will be $\langle d \rangle = 2 w_i R_i$.

Although the data are readily fitted with this number of parameters, a useful model-independent quantity, the integrated intensity, often referred to as an "invariant,"[33] can be extracted from the data for comparison to model calculations. Here we compute two integrated intensities from the fits to the data: Q_L, for comparison with surface roughness data, and Q_N, for study of the bulk nanostructure in Sec. V:

$$Q_L = 4\pi \int q^2 I_L dq, \tag{8}$$

$$Q_N = 4\pi \int q^2 I_N dq. \tag{9}$$

In these equations the limits of integration are from $q=0$ to $q=\infty$, which is possible here based on extrapolating the fitted functions beyond the experimental range. The factor of 4π results from the angular integration over all angles under the assumption of isotropic scattering. Note that integration yields $Q_L = \pi^2 b$ based on Eq. (6).

The solid lines through the data in Fig. 3 are fits of Eq. (7) with the parameters listed in Table II. An extremely small contribution from nanoscale features is found for 1H compared to a rather large contribution for 1D. This is reflected in the more than two orders-of-magnitude increase in Q_N. Also, the b parameter and Q_L show a larger contribution from the larger-scale features in 1D. The a parameter indicates a slightly larger correlation length for 1D compared to 1H, although both are quite large and consistent with Porod-like behavior.

Figures 4–6 show the SANS data and fits for the other six samples investigated, in pairs without/with D for easy comparison. All data show features noted above with steep decreases at the lowest q's and approaches to near constant values at high q. In addition, there is clear evidence of nanostructural features in the intermediate q range for most of the samples in Figs. 4–6 but none show the strong SANS intensities seen for 1D. There is more scatter apparent in the data in the region of q around 0.2 nm^{-1}. This is where the data from the two detector positions overlap and the intensity at the 13-m position is extremely weak in this q range.

Values of the fitted parameters for all samples are included in Table II. The values of I_{inc} can be compared with the theoretical values, I_{inc}(th), based on Eq. (1) as listed in the last column of Table II. The excellent agreement indicates the accuracy of the H and D concentrations obtained from the IR analysis as well as the accuracy of the experimental SANS absolute intensity values, based on the total film thicknesses listed in Table I. The fit results show that the nanostructural objects average from 4 to 8 nm, while the larger scale features are at least 20 nm in size. It is important to note the differences in the Q_N values between the H-containing films and the D-containing films, in particular, the significant reduction in Q_N for the two films with *partial*

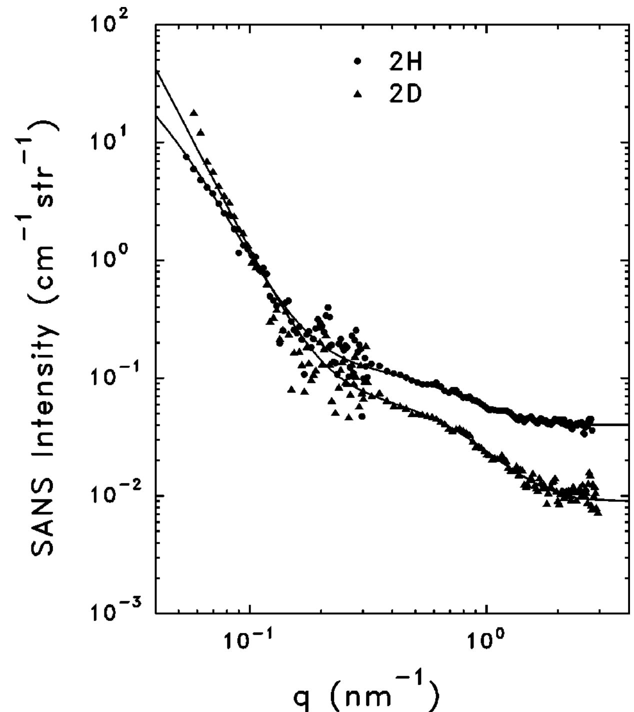

FIG. 4. SANS from samples 2H and 2D. Solid lines are fits to data based on Eq. (7).

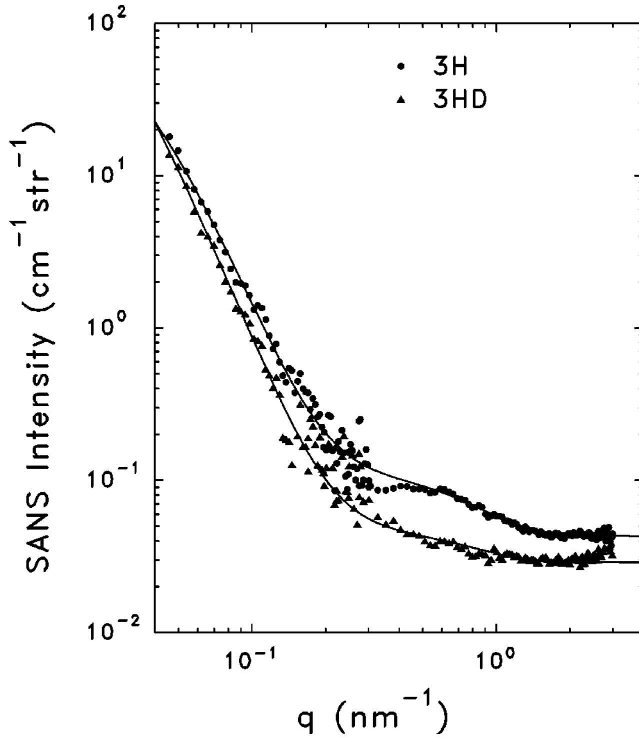

FIG. 5. SANS from samples 3H and 3HD. Solid lines are fits to data based on Eq. (7).

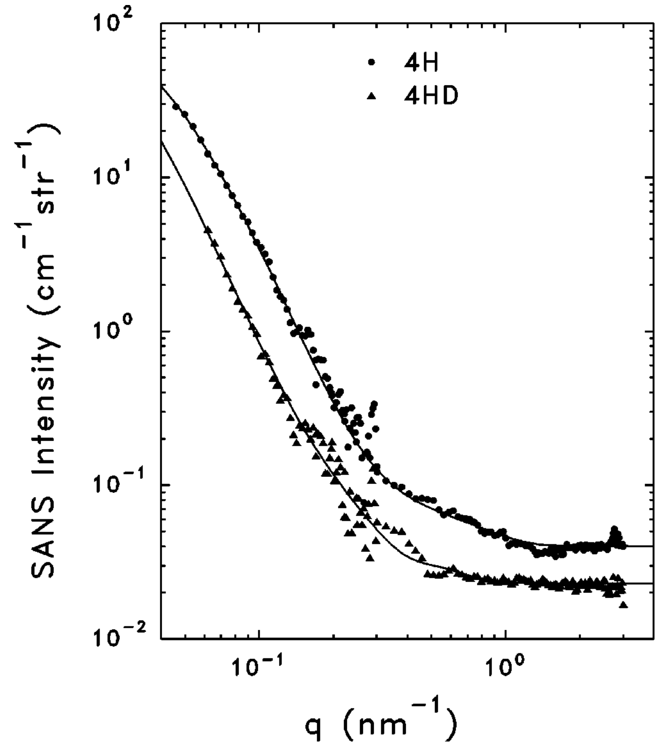

FIG. 6. SANS from samples 4H and 4HD. Solid lines are fits to data based on Eq. (7).

D replacement of H. This is a clear indication that some aspect of the H distribution is nonuniform.

IV. SAXS RESULTS

The SAXS results from the four companion samples deposited on Al foil are summarized in Table III. The shape of the SAXS intensity versus q was similar to that for the SANS from 1H (Fig. 3) for all four samples. The data are well fitted with a Porod term plus a constant term,

$$I_{\mathrm{SAXS}}=P_s/q^3+I_{\mathrm{diff}}, \tag{10}$$

where the units are electrons/atom [also known as electron units (eu) typical for SAXS]. Note that the Porod term behaves as q^{-3} rather than as q^{-4} in Eq. (2) since the SAXS system uses a line-slit geometry.[24] The diffuse scattering I_{diff}, known as the Laue monotonic scattering,[24,35] is due to electron density fluctuations on the atomic scale and increases with H content.[35] The effect of D on I_{diff} should be nearly identical to H based on the theory,[24,35] consistent with the values listed in Table III. Comparing the P_s values in Table III with the b values in Table II, 1D shows the strongest Porod scattering in both SANS and SAXS, and the 2H, 2D pair show weaker Porod scattering than 1H. There is no evidence of a contribution from nanoscale features in the SAXS data. Based on the statistical scatter in the data at high q, we can calculate maximum Q_N's (in the same units as the SANS Q_N) for two different average diameters of scattering objects (Table III). This is done since the small-angle intensity becomes less sensitive as the objects become smaller [see Eq. (4)]. These values can be used to place an upper limit on the microvoid fractions in the films. The lack of a detectable Q_N for sample 1D from the SAXS data, in contrast to the strong Q_N from the SANS sample, is likely related to the differences in microcrystallinity in these two companion samples deposited on different substrates (Al foil vs c-Si). This difference will not be an issue since sample 1D will not be crucial in testing the proposed a-Si:H two-domain model. The partial microcrystallinity of the SANS 1D sample will, however, be carefully considered.

V. INTERPRETATION AND DISCUSSION

Our interpretation of the SANS results is based on some general expressions related to the nonuniformity of the samples described in terms of "phases." Examples are microvoids and a homogeneous a-Si:H matrix, or high-H regions and low-H regions of the a-Si:H matrix, or the a-Si:H matrix and microcrystalline inclusions, etc. Using this approach, the integrated intensity, Eq. (8) or (9), can be com-

TABLE III. SAXS results from four companion films. Column labels defined in text.

Sample	P_s (eu/nm^3)	I_{diff} (eu)	Q_N ($\geqslant$3 nm, $\leqslant$10 nm) (10^{21} cm^{-4})	Q_N ($\leqslant$2 nm) (10^{21} cm^{-4})
1H	4.5	12	$\leqslant$1	$\leqslant$3
1D	28	13	$\leqslant$1	$\leqslant$3
2H	1.8	16	$\leqslant$2	$\leqslant$6
2D	1.2	16	$\leqslant$2	$\leqslant$6

TABLE IV. Scattering length densities, ρ, useful for modeling. ρ_m is the mass density.

Phase or Sample	ρ_m (g/cm^3)	ρ (10^{10} cm^{-2})
c-Si	2.33	2.07
a-Si (no H)	2.29	2.04
Void (0 atm or 1 atm H_2 or D_2)	0.00	0.00
Void (10 kbar H_2)	0.14[a]	−3.12
Void (10 kbar D_2)	0.28[a]	5.58
1H	2.22	1.75
1D	2.20	2.40
2H	2.21	1.69
2D	2.20	2.40
3H	2.19	1.63
3HD	2.19	1.98
4H	2.21	1.70
4HD	2.21	1.98

[a]Fluid normal-H_2 (and normal-D_2) density from Ref. 37.

puted on the basis of two-phase or three-phase models.[33] For two phases,

$$Q=(2\pi)^3(\rho_1-\rho_2)^2\Phi(1-\Phi), \tag{11}$$

where ρ_1, and ρ_2 are the neutron scattering length densities of the two phases and Φ, $(1-\Phi)$ are the volume fractions of the two phases. The inherent assumption is that the sizes of the scattering features are in the range probed by SANS. Similarly, for three phases,

$$Q=(2\pi)^3[(\rho_1-\rho_2)^2\Phi_1\Phi_2+(\rho_1-\rho_3)^2\Phi_1\Phi_3 + (\rho_2-\rho_3)^2\Phi_2\Phi_3], \tag{12}$$

where Φ_1, Φ_2, and Φ_3 are the volume fractions of the three phases $(\Phi_1+\Phi_2+\Phi_3=1)$. Note that Eq. (12) reduces to Eq. (11) for $\Phi_3=0$.

The scattering length density of a phase can be computed from its mass density, atomic composition, and the known neutron scattering lengths,[32] b_i of each element in the phase,

$$\rho=N_A\rho_m\sum x_ib_i \Big/ \sum x_iW_i, \tag{13}$$

where N_A is Avogadro's number, ρ_m is the mass density, x_i is the atomic fraction of element *i*, and W_i is the atomic weight of element *i*. Here lies the important sensitivity of SANS for the study of H uniformity of *a*-Si:H: the negative sign of $b_H(-3.74\times10^{-13}$ cm) versus the positive sign of b_D $(+6.67\times10^{-13}$ cm) and b_{Si} $(+4.15\times10^{-13}$ cm), as well as the comparable magnitudes of b_H, b_D, and b_{Si}. Table IV provides some values of ρ for various phases of interest, including those with homogenous amorphous matrices for the eight SANS samples. The inclusion of the high-pressure H_2 and D_2 in voids is included based on the detection of such objects with pressure in the 10-kbar range as reported in Ref. 16.

To find the scattering length densities of the SANS samples, the mass densities used (Table IV) are based on an experimentally determined correlation between H content, C_H (in at.%), and flotation density[24] measured in our laboratory for many *a*-Si:H films covering a wide range of C_H:

$$\rho_m(\text{g/cm}^3)=2.291-0.0068C_H, \tag{14}$$

The extrapolated value of 2.291 g/cm^3 for *a*-Si agrees with the measured result that the density of void-free *a*-Si is 1.8% less than that of *c*-Si.[36] Based on Eq. (14), it is assumed that the behavior of deuterated films will be

$$\rho_m=2.291-0.0066C_D, \tag{15}$$

based simply on the increased mass of D, i.e., the mass change compared to Si will be about 1/28 smaller than the 0.0068 slope in Eq. (14). From Eqs. (14) and (15) and the H and D compositions in Table I, the values of ρ for each sample are computed from Eq. (13) and listed in Table IV. Note that each of these represent an *average* ρ assuming a homogenous film.

TABLE V. Estimated surface roughness from SANS Q_L compared to AFM data. Uncertainties are approximately 20% of the values listed.

Sample	Φ_s	R_{rms} (AFM)/thickness
1H	0.0024	0.0024
1D	0.014	0.012

A. Surface roughness

To obtain the data presented previously SANS was performed through stacked thin films. Because of the significant sample surfaces present in these measurements, their possible influence on the results must be carefully taken into account. The possible importance of surface imperfections in SANS was shown several years ago[38] and a Porod (q^{-4}) dependence was documented, similar to our data at low *q*. The role of surface roughness can be estimated if we assume that deviations from a perfectly smooth surface can be approximated with voids (of arbitrary shape) on the surface. It is assumed that the SANS contributions from the larger-scale features, Q_L listed in Table II, are due to surface roughness because their size (>20 nm) compares well to the AFM evidence of lateral roughness. This assumption can be tested by estimating the *vertical* surface roughness R_{rms} to compare with the AFM results for samples 1H and 1D (4.7 and 20 nm, respectively). From Eq. (11) with $\rho_1=0$ for voids and $\rho_2=\rho$, the average value for each sample as listed in Table IV, the effective surface void volume fractions are listed as Φ_s in Table V. One measure of the surface void fraction is simply the ratio of rms roughness to the film thickness (2.0 and 1.7 μm, respectively) and this is listed in Table V for the two samples with available AFM results. The agreement between this measure and those predicted from Q_L is excellent. The Φ_s for the other samples are all smaller, suggesting smoother surfaces for these samples prepared with the different conditions listed in Table I. If the Φ_s from the other samples are converted into estimated R_{rms} from the product of Φ_s and

film thickness, values of 1–3.2 nm are found based on these SANS data. The rougher surface of 1D is perhaps due to the formation of partially microcrystalline material as documented in Fig. 2. None of the other samples are as rough as 1D, consistent with the lack of any detected microcrystallinity. However, as noted in Table III the SAXS results showed evidence of a rougher surface for sample 1D (larger P_s), even though no microcrystallinity was detected by XRD in the SAXS sample deposited on the Al foil. From SANS on the other pairs, there is no clear evidence of a trend toward smoother surfaces using H- or D-containing source gases, although both pairs prepared with disilane show improved smoothness (smaller Q_L) with D_2 dilution versus H_2 dilution.

Other AFM studies of surface roughness of *a*-Si:H films grown by PECVD observed R_{rms} values and lateral sizes similar to those detected here for comparable film thickness (~1–2 μm).[39–42] In Ref. 41, experimental data show that the roughness of microcrystalline films is significantly larger than amorphous films of similar thickness, about 3.5 nm vs 0.75 nm at 1-μm thickness. It is interesting that earlier SANS studies did not attribute evidence of larger scale features to surface roughness.[13,14,16] The results from Guy *et al.*[16] yielded a Porod-like behavior with intensities similar to those observed here. Although the film was removed from the substrate and in powder form for this study, the surface roughness will have been preserved.

B. Test of two-domain model for samples 1H and 1D

The origin of the nanostructural features, quantified by Q_N and $\langle d \rangle$, defined in Sec. III and listed in Table II, is now considered. First the two-domain model[9,10] is developed as a three-phase model with the following volume fractions and scattering length densities: high-density amorphous matrix (Φ_a, ρ_a), low-density amorphous boundary (Φ_b, ρ_b), and paracrystals with a *c*-Si-like behavior (Φ_c, ρ_c). Based on the latest version of the proposed two-domain model,[10] with paracrystals in the 1–3-nm size range, the following values of these parameters are tested for sample 1H: $\Phi_a = 0.75$, $\Phi_b = 0.15$, $\Phi_c = 0.10$, and $\rho_a = 1.83 \times 10^{10}\ \text{cm}^{-2}$ (assuming 8-at. % H in this high-density matrix phase), $\rho_b = 1.00 \times 10^{10}\ \text{cm}^{-2}$ (assuming the balance of the H is in this low-density boundary region, yielding 33 at. % based on volume fractions), and $\rho_c = 2.04 \times 10^{10}\ \text{cm}^{-2}$ [assuming the paracrystals contain no H and have a density identical to H-free *a*-Si (Table IV)]. Note that these choices yield an average mass density (2.22 g/cm^3, Table IV), an average H content (11 at. %, Table I), and about half the H in the boundary regions as in the two-domain model.[10] The latter fraction is consistent with the typical fraction in the NMR clustered phase for PECVD material. Substituting these values into the three-phase model, Eq. (12), yields $Q_N = 2.41 \times 10^{21}\ \text{cm}^{-4}$, more than two orders of magnitude larger than the experimental result of $0.01 \times 10^{21}\ \text{cm}^{-4}$ (Table II). In fact, a small microvoid fraction of only 0.01% of unpressurized voids or 0.002% of 10-kbar H_2 pressurized voids (see Table IV for ρ's) would result in the observed Q_N.

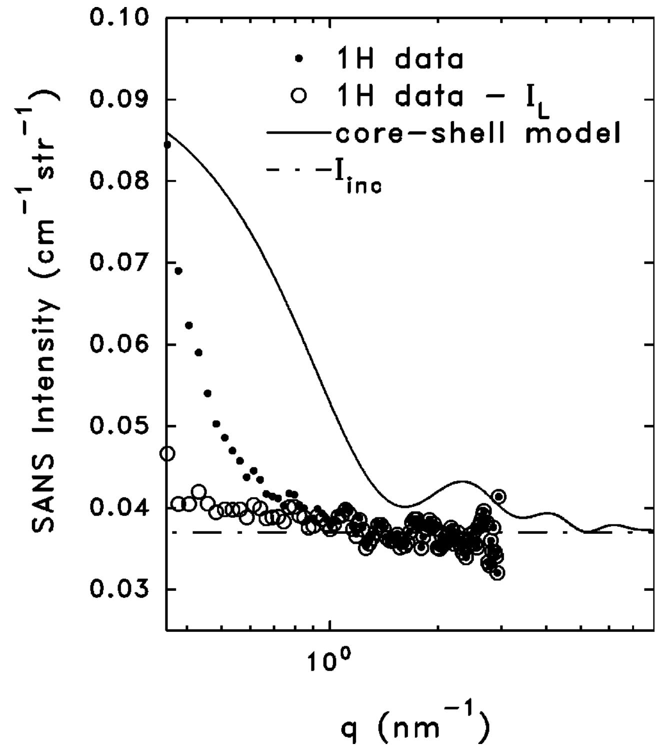

FIG. 7. Comparison of SANS data from sample 1H and a core-shell model calculation to simulate the two-domain model. The fit of I_L from Eq. (6) has been used to remove the surface roughness contribution from the data, leaving only $I_N + I_{\text{inc}}$ to compare with the calculation.

To predict the shape and magnitude of the SANS intensity in the two-domain model compared to the actual data in Fig. 3 for sample 1H, we use a spherical core-shell model with paracrystals having 1–3-nm-diameter cores and 0.2–0.5 nm thick boundary layers, imbedded in the amorphous matrix.[10] Dimensions are selected to yield the volume fractions used above. The SANS intensity for spherical core shells can be calculated from[43]

$$I_N = C[(\rho_b - \rho_a) V_T F(qR_T) + (\rho_c - \rho_b) V_c F(qR_c)]^2, \tag{16}$$

where $F(qR_i)$ is the form factor for a sphere as given earlier in Eq. (5), V_c is the volume of the spherical paracrystal, V_T is the total volume of the paracrystal core plus boundary shell, and C is a constant that can be adjusted to give the same Q_N as the three-phase model. Values of $R_c = 0.5$, 1.0, and 1.5 nm are used with equal number densities to create a rough distribution of spherical paracrystals in the proposed size range. The corresponding boundary thicknesses that yield the 15% volume fraction are 0.18, 0.36, and 0.50 nm, respectively. The result is compared with the sample 1H experimental data in Fig. 7. The contribution from the surface roughness, I_L, has been subtracted from the experimental data and only the higher q region of the data is shown since this is the region where objects of the proposed size will produce a SANS intensity that varies with q. The strong oscillations in the calculated I_N are due to interference effects associated with the spherical core-shell model for these

TABLE VI. Calculation of Q_N from two- or three-phase models for sample 1D. The experimentally observed $Q_N = 2.15\times10^{21}$ cm^{-4} (Table II). Column labels are defined in text.

Parameter set	Φ_a	Φ_b	Φ_c	ρ_a (10^{10} cm^{-2})	ρ_b (10^{10} cm^{-2})	ρ_c (10^{10} cm^{-2})	Q_N (10^{21} cm^{-4})
A	0.88	0	0.12	2.46	-	2.07	0.40
B	0.83	0.05	0.12	2.40	3.81	2.07	2.77
C	0.78	0.10	0.12	2.40	3.01	2.07	1.24
D	0.87	0.01	0.12	2.47	0	2.07	1.86
E	0.87	0.01	0.12	2.41	5.58	2.07	2.83

choices of radii and boundary thicknesses; a more continuous size distribution would tend to wash these out. The discrepancy between the data and the core-shell model calculation shows that the two-domain model[9,10] does not describe the morphology of sample 1H. This particular sample is one that is near the onset of microcrystallinity since it was prepared under the high H_2 dilution, a condition that produced partial microcrystallinity when switched to the deuterated gases for sample 1D. However, we note that a somewhat lower dilution coupled with a somewhat higher plasma power was used for 1D to yield a similar deposition rate to 1H, so the exact mechanism for the partial microcrystallinity of 1D is unknown. Others have shown that D can lower the partial pressure at which the amorphous-microcrystalline transition occurs.[44] The microstructural quality of sample 1H is also indicated by the low value of $R = 0.12$ from the IR analysis (Table I).

A two-domain (or three-phase) model may, however, be appropriate to explain the sample 1D data since the above calculated $Q_N = 2.41\times10^{21}$ cm^{-4} is close to the observed $Q_N = 2.15\times10^{21}$ cm^{-4} (from Table II) and the XRD result (Fig. 2) indicated approximately 12 vol. % of microcrystals. Also, the size of the microcrystals estimated from the Scherrer equation[20] and the width of the (220) XRD line in Fig. 2 gives 8 nm, in excellent agreement with the average size $\langle d \rangle = 8$ nm (Table II) from the SANS analysis. Other evidence of a defective, H-rich layer around the microcrystallites in mixed amorphous-microcrystalline Si:H material has been reported.[45–47] To examine the SANS more carefully, calculation of Q_N is done for the various sets of parameters in Table VI. Parameter set *A* assumes only microcrystals and homogeneous amorphous matrix. The 13-at. % D from the IR (Table I) is assumed to be located only in the amorphous matrix (thus the concentration there increases to 15 at. %), the scattering length density is found from Eqs. (13) and (15) and the microcrystals are assumed to behave as *c*-Si (Table IV). This set clearly underestimates the integrated SANS intensity by factor of 5. Sets *B* and *C* assume that deuterium is expelled from the *c*-Si inclusions and accumulates in a boundary region such that the concentrations are 44 and 29 at. % for $\Phi_b = 0.05$ and 0.10, respectively. One can see that Q_N is quite sensitive to the Φ_b and a value of 0.06 with 39-at. % D will reproduce the observed Q_N. This high concentration is consistent with an optical absorption study of partially microcrystalline Si:H films,[45] which finds evidence of 38-at. % H in the boundary region of crystallites below 20 nm in size. However, a boundary layer thickness of 1.8 nm, independent of crystallite size is found in their modeling.[45] This would correspond to a large value of $\Phi_b = 0.36$ for the average 8-nm-diameter crystallites, much larger than the $\Phi_b = 0.06$ required here to fit the SANS Q_N. The latter volume fraction implies a boundary layer thickness of about 0.6 nm.

In an alternative approach, parameter sets *D* and *E* assume microvoids rather than a boundary region. Using voids at 0 or 1 atm D_2 (set *D*), only slightly more than 1 vol. % is needed to produce the observed Q_N, while about 0.7 vol. % of 10 kbar D_2 pressurized voids (set *E*) is needed.

The SANS from 1D can therefore be explained by *c*-Si inclusions either surrounded by D-rich boundary regions or

TABLE VII. Two-domain model calculations. Volume fractions of $\Phi_a = 0.75$, $\Phi_b = 0.15$, and $\Phi_c = 0.10$ are used. Two distributions of H/D in the three phases (a:b:c) are assumed: 55%:45%:0% and 65%:35%:0%. The associated scattering length densities of the amorphous matrix and the boundary layer are shown. The paracrystals are assumed to have $\rho_c = 2.04\times10^{10}$ cm^{-2} in every case.

	55%:45%:0% H/D distribution			64%:36%:0% H/D distribution		
Sample	ρ_a (10^{10} cm^{-2})	ρ_b (10^{10} cm^{-2})	Q_N (10^{21} cm^{-4})	ρ_a (10^{10} cm^{-2})	ρ_b (10^{10} cm^{-2})	Q_N (10^{21} cm^{-4})
1H	1.83	1.00	2.41	1.79	1.24	1.20
2H	1.79	0.75	3.75	1.74	1.06	1.81
2D	2.30	3.51	5.01	2.34	3.12	2.30
3H	1.75	0.42	6.07	1.70	0.86	2.70
3HD	2.00	1.88	0.06	1.99	1.91	0.03
4H	1.80	0.79	3.53	1.76	1.11	1.65
4HD	1.99	1.88	0.05	1.98	1.90	0.03

in combination with microvoids. Note that the IR microstructure factor R is significantly larger for 1D compared to 1H (Table I), indicating more Si-D_2-type bonding and/or Si-D bonding on internal microvoid surfaces.[27–30] It is also possible that *both* voids and D-rich boundary regions are present. Evidence of more that 1 vol. % of microvoids in predominantly microcrystalline Si:H films has been found from small-angle *x*-ray scattering experiments, combined with flotation density measurements.[48] Spherelike voids up to 10 nm in diameter have also been imaged in microcrystalline Si:H by transmission electron microscopy.[49]

C. Test of two-domain model for samples 2H to 4HD

We now consider the data from the remaining samples 2H, 2D, 3H, 3HD, 4H, and 4HD. Table II and Figs. 4–6 show that the Q_N's of 2H, 3H, and 4H are significantly larger than for 1H, while the two samples with the H/D mixtures (3HD and 4HD) show significant reductions in Q_N compared to their companions containing only H. Based on the two-domain model,[10] with the same volume fractions and H distribution among the paracrystals, boundaries, and amorphous matrix as used for 1H, calculations of Q_N from Eqs. (12)–(15) are summarized in Table VII. For the mixed H/D samples, fractions of H/D equal to the atomic concentrations shown in Table I are assumed in both the amorphous matrix and boundary region. A second scenario of a smaller amount of H/D in the boundary regions (reduced from 45% to 36%) is included to indicate the sensitivity of Q_N to this split.

Several features within Table VII are noteworthy. For samples 2H and 2D, the Q_N's for both scenarios are approximately an order of magnitude larger than the experimental values (Table II) and the 2D value is predicted to be significantly larger than the 2H value. For samples 3H and 4H, the Q_N's are more than an order of magnitude too large, but for the H/D mixed samples 3HD and 4HD, the effect of "contrast variation," [33] enabled by the opposite signs of the scattering lengths of H and D, is predicted to drastically reduce the Q_N's. This approach was previously employed to demonstrate H non-uniformity in sputter-deposited *a*-Si:H/D.[8,14] Figure 8 shows the dependence of the scattering length densities on H+D contents for all the samples and illustrates the weak dependence of ρ for samples 3HD and 4HD with fractions of D to H at the values listed in Table I. The experimental Q_N's for 3HD and 4HD do show a significant reduction compared to their 3H and 4HD counterparts (Table II), suggesting a contrast matching effect. However, due to the poor general agreement of the Q_N's, as well as in the sizes of the scattering features (Table II), with the two-domain model

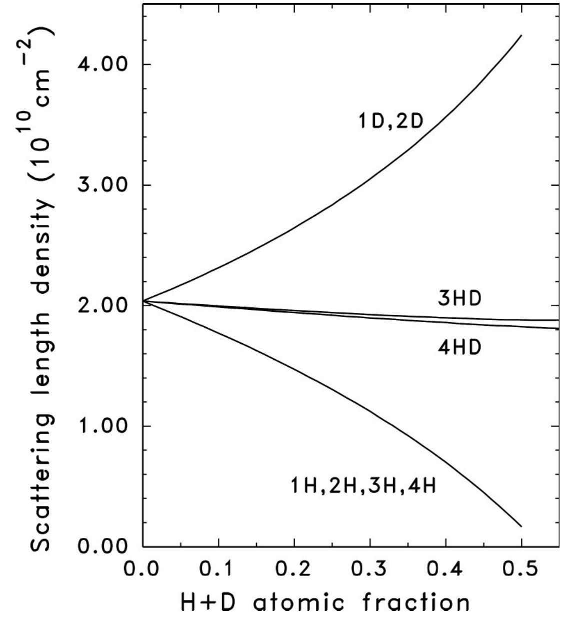

FIG. 8. Scattering length densities ρ calculated from Eqs. (13)–(15) as a function of H+D concentrations. For samples 3HD and 4HD, the ratios of D to H were fixed to the values found from IR analyses (Table I).

predictions, alternate models are now considered to search for H nanostructures that more closely match the experimental data.

D. Microvoid model

Due to the likely presence of small fractions of microvoids, we first analyze the SAXS results from Table III to place an upper limit on the void fractions in the four companion samples studied by SAXS. Equation (11) can be used with the appropriate scattering length density for SAXS,

$$\rho_x = n\sigma_e^{1/2}, \tag{17}$$

where n is the number density of electrons and σ_e is the electron x-ray (Thomson) cross section $= 7.94\times10^{-26}\ cm^2$. To calculate n for the amorphous matrix of each sample we take the electron density of *c*-Si (7.0×10^{23}) times the ratio of the mass density of the film to that of *c*-Si. We consider two extremes of H_2/D_2 pressure, P, within the microvoids, 0 atm and 10 kbar. Evidence of pressures in the 10-kbar range at room temperature has been reported for *a*-Si:H.[16] Table VIII presents the upper limit on void fractions of the two size ranges considered in Table III for estimating the upper limits

TABLE VIII. Upper limits of microvoid volume fractions in % based on SAXS results.

Sample	Φ_v ($P=0$ atm) (≥3 nm, ≤10 nm)	Φ_v ($P=10$ kbar) (≥3 nm, ≤10 nm)	Φ_v ($P=0$ atm) (≤2 nm)	Φ_v ($P=10$ kbar) (≤2 nm)
1H	≤0.01	≤0.02	≤0.03	≤0.05
1D	≤0.01	≤0.02	≤0.03	≤0.05
2H	≤0.02	≤0.03	≤0.06	≤0.09
2D	≤0.02	≤0.03	≤0.06	≤0.09

TABLE IX. Calculated microvoid volume fractions, Φ_v, assuming all of SANS Q_N is due to voids, and assuming either low (0 or 1 atm) or high (10 kbar) pressures of H_2/D_2 in the voids. Experimental Q_N's from Table II are used in Eq. (11) to find Φ_v.

Sample	Φ_v (at 0 or 1 atm) (vol. %)	Φ_v (at 10 kbar) (vol. %)	P (kbar)	Φ_v (at P) (vol. %)
1H	0.013	0.002	-	-
1D	1.53	0.86	-	-
2H	0.50	0.062	1 or 14	0.35 or 0.04
2D	0.22	0.13	1 or 14	0.35 or 0.04
3H	0.34	0.041	4.5	0.10
3HD	0.08	0.15	4.5	0.10
4H	0.13	0.016	10	0.02
4HD	0.010	0.015	10	0.02

on Q_N (SAXS). It is clear that the void volume fractions must be quite low in these high-quality films.

Next consider whether voids containing low pressure (0 or 1 atm) or high-pressure H_2/D_2 (10 kbar) can explain the SANS Q_N's and their changes upon deuteration. In this case, the two-phase model [Eq. (11)] is used with the scattering length densities listed in Table IV to find the void fraction Φ_v for the two pressures. Results are listed in Table IX, including calculations for 1H and 1D.

Comparing the SAXS and SANS void interpretations in Tables VIII and IX, a discrepancy is obvious for sample 1D and this can be attributed to the partial microcrocrystallinity present only in the SANS sample (considered earlier in Table VI calculations). Regarding the possible void sizes in Table VIII, the SANS analyses of Table II show that sizes greater than 3 nm should be considered. Using these upper limit columns, only sample 1H seems to be consistent with a void-only interpretation. Even the high-pressure scenarios for 2H and 2D yield larger void fractions from the SANS data than allowed by the SAXS upper limits. Although it appears that a void-only interpretation is not likely, it seems reasonable that the void fractions could be somewhat higher in the 3H/3HD pair than in the 4H/4HD pair due to the lower substrate temperature used in preparation (Table I). If we assume that the D-and H-containing samples of each pair have the same void volume fraction (except for 1H, and 1D), then the pressure P inside the voids can be adjusted to generate the experimental Q_N's for the pair. The last two columns of Table IX show such pressures and the associated void fractions. Note that under this assumption, the void fractions for 2H and 2D at $P=14$ kbar are now only slightly above the SAXS upper limit. Such pressures are consistent with the analysis of earlier SANS results,[16] but the sizes found in Table II are much larger than their 1.3-nm-diameter "cages,"[16] The material analyzed in this study[16] however was significantly different than ours, prepared with much higher H/D concentrations (22/23 at. %) and void fractions (>1 vol. %).

E. H/D composition fluctuation model

Finally, we consider a simple two-phase heterogeneity based on an amorphous matrix with two different bonded H/D contents, one phase slightly lower than the average H/D content (Table I), representing the bulk of the *a*-Si:H/D, and the other representing a H/D-rich phase. We then explore what combinations of volume fractions and H/D concentration differences are required to generate the observed Q_N's (Table II). To work with reasonable estimates of the volume fraction of the H/D-rich phase, we make one of two assumptions: (a) the volume fraction is given by the R value found from the IR analyses as listed in Table I, or (b) the volume fraction is at a maximum of 50%. The former assumption is supported by a correlation of NMR clustered-phase signal and the IR intensity of the 2080-cm^{-1} mode.[50,6] The latter assumption yields the minimum possible contrast since $\Phi(1-\Phi)$ will be the maximum possible value. A 50% fraction is not unreasonable since NMR has often yielded clustered-phase fractions of this magnitude or even greater.[4,50,51] The scattering contrast between the two phases, $\Delta\rho$, is then calculated from Eq. (11) and compared with the calculations in Fig. 8 to extract the difference in H/D concentration, $\Delta C_{H/D}$, to determine if either of the two assumptions are feasible. Table X lists the results.

The H/D composition fluctuations indicated by the calculations for either scenario in Table X are quite large except for sample 1H, which exhibits the best uniformity of the set. Sample 3HD could not be fitted with this model since $\Delta\rho$ is larger than allowed as seen in the weak H/D dependence in Fig. 8. This suggests that at least part of Q_N must be due to another scattering mechanism. Also, the $\Delta C_{H/D}$ calculated for 4HD is much larger than its companion 4H; however the uncertainty is large since Q_N is so small (0.01

TABLE X. Scattering length density contrasts and H/D concentration fluctuations under two-phase model assumptions.

Sample	$\Phi(1-\Phi)$ IR	$\Delta\rho$ (10^{10} cm^{-2})	$\Delta C_{H/D}$ (at. %)	$\Phi(1-\Phi)$ (max.)	$\Delta\rho$ (10^{10} cm^{-2})	$\Delta C_{H/D}$ (at. %)
1H	0.11	0.06	2	0.25	0.04	1
2H	0.16	0.30	10	0.25	0.24	8
2D	0.18	0.27	8	0.25	0.22	7
3H	0.14	0.26	9	0.25	0.19	7
3HD	0.18	0.13	Not feas.	0.25	0.11	Not feas.
4H	0.11	0.18	6	0.25	0.12	4
4HD	0.14	0.05	12	0.25	0.04	8

$\times 10^{21}$ cm^{-4}) and near the detection limit. In the cases of the 3H/3HD or 4H/4HD pairs, a small fraction of microvoids could bring each pair into consistency such that the H/D composition fluctuations are similar and in the 5–10% range. Samples 3H/3HD would require a larger void fraction but this would be consistent with the lower substrate temperature used in preparation (Table I).

VI. SUMMARY AND CONCLUSIONS

A series of eight PECVD films, prepared in pairs with and without D substitution, has been investigated by SANS and several other complementary techniques (SAXS, IR, AFM, XRD). Careful sample design allowed SANS measurement of relatively thin, device-quality films. In general, SANS features from all samples could be divided into sizes that were relatively large (>20 nm) and relatively small (<8 nm). The scattering from smaller scale features was generally weak except for one sample that exhibited partial microcrystallinity. Good evidence was presented for the assignment of the larger features to film surface roughness, a mechanism not previously identified in SANS studies of similar materials to our knowledge. No single hypothesis could unequivocally describe the smaller scale features due to the general weakness of the scattering and at least two possible contributing mechanisms: microvoids and H/D-rich clusters. Microvoid-only or H/D cluster-only interpretations are not capable of explaining all the data so that mixtures of the two features are likely present. A careful analysis in terms of a proposed two-domain model[9,10] involving small crystallinelike Si domains surrounded by H/D-rich boundaries showed that this model is generally untenable due to the absence of strong neutron scattering associated with the expected high H/D nonuniformity on the nanoscale.

ACKNOWLEDGMENTS

We are grateful for the technical assistance of B. Hammouda at the NCNR with the SANS experiments, to H. Moutinho, of NREL for the AFM measurements, and to L. Gedvilas and B. Keyes of NREL for the FTIR measurements. This research was supported by a subcontract from NREL (No. XAK-8-17619-31). The work at United Solar was supported in part by NREL (No. ZAK-8-17619-09). We also acknowledge the support of the National Institute of Standards and Technology, U.S. Department of Commerce, in providing the neutron research facilities used in this work.

*Author to whom correspondence should be addressed. Electronic mail: dwilliam@mines.edu

[1] D. V. Tsu, B. S. Chao, S. R. Ovshinski, S. Guha, and J. Yang, Appl. Phys. Lett. **71**, 1317 (1997).

[2] P. M. Voyles, M. M. J. Treacy, H-C. Jin, J. R. Abelson, J. M. Gibson, J. Yang, S. Guha, and R. S. Crandall, in *Amorphous and Heterogeneous Silicon Thin Films-2000*, edited by R. W. Collins, H. M. Branz, M. Stutzmann, S. Guha, and H. Okamoto, MRS Symposia Proceedings No. 609 (Materials Research Society, Pittsburgh, 2000), p. A2.4.

[3] D. V. Tsu, B. S. Chao, S. R. Ovshinsky, S. J. Jones, J. Yang, S. Guha, and R. Tsu, Phys. Rev. B **63**, 125338 (2001).

[4] J. B. Boyce and S. E. Ready, Physica B **170**, 305 (1991), and references therein.

[5] Y. Wu, J. T. Stephen, D. X. Han, J. M. Rutland, R. S. Crandall, and A. H. Mahan, Phys. Rev. Lett. **77**, 2049 (1996).

[6] D. Han, J. Baugh, G. Yue, and Q. Wang, Phys. Rev. B **62**, 7169 (2000).

[7] J. Baugh, D. Han, A. Kleinhammes, and Y. Wu, Appl. Phys. Lett. **78**, 466 (2001).

[8] A. Menelle, J. Non-Cryst. Solids **97&98**, 337 (1987).

[9] J. Baugh and D. Han, in *Amorphous and Heterogeneous Silicon-Based Films-2001*, edited by M. Stutzmann, J. B. Boyce, J. D. Cohen, R. W. Collins, and J. Hanna, MRS Symposia Proceedings No. 664 (Materials Research Society, Pittsburgh, 2001), p. A19.1.

[10] J. Baugh and D. Han, Phys. Rev. B **66**, 115203 (2002).

[11] T. Gotoh, S. Nonomura, M. Nishio, S. Nitta, M. Kondo, and A. Matsuda, Appl. Phys. Lett. **72**, 2978 (1998).

[12] P. M. Voyles, N. Zotov, S. M. Nakhmanson, D. A. Drabold, J. M. Gibson, M. M. J. Treacy, and P. Keblinski, J. Appl. Phys. **90**, 4437 (2001).

[13] A. J. Leadbetter, A. A. M. Rashid, R. M. Richardson, A. F. Wright, and J. C. Knights, Solid State Commun. **33**, 973 (1980).

[14] R. Bellisent, A. Chenevas-Paule, and M. Roth, J. Non-Cryst. Solids **59&60**, 229 (1983); Physica B **117&118**, 941 (1983).

[15] A. Chenevas-Paule, R. Bellisent, M. Roth, and J. I. Pankove, J. Non-Cryst. Solids **77&78**, 373 (1985).

[16] C. A. Guy, A. F. Wright, R. N. Sinclair, R. J. Stewart, and F. Jansen, J. Non-Cryst. Solids **196**, 260 (1996).

[17] D. L. Williamson, D. W. M. Marr, B. P. Nelson, E. Iwaniczko, J. Yang, B. Yan, and S. Guha, in *Amorphous and Heterogeneous Silicon Thin Films-2000* (Ref. 2), p. A16.2.

[18] R. Bellisent, in Amorphous Silicon and Related Materials, edited by H. Fritzche (World Scientific, Singapore, 1988), p. 93.

[19] J. Yang, A. Banerjee, and S. Guha, Appl. Phys. Lett. **70**, 2975 (1997).

[20] D. L. Williamson, in *Amorphous and Heterogeneous Thin Films: Fundamentals to Devices-1999*, edited by H. M. Branz, R. W. Collins, H. Okamoto, S. Guha, and R. Scrropp, MRS Symposia Proceedings No. 557 (Materials Research Society, Pittsburgh, 1999), p. 251.

[21] D. L. Ho, R. M. Briber, R. L. Jones, S. K. Kumar, and T. P. Russel, Macromolecules **31**, 9247 (1998).

[22] C. J. Glinka, J. G. Barker, B. Hammouda, S. Kreuger, J. J. Moyer, and W. J. Orts, J. Appl. Crystallogr. **31**, 430 (1998).

[23] J. G. Barker (private communication).

[24] D. L. Williamson, in *Amorphous Silicon Technology-1995*, edited by M. Hack, E. A. Schiff, A. Madan, M. Powell, and A. Matsuda, MRS Symposia Proceedings No. 377 (Materials Research Society, Pittsburgh, 1995), p. 251.

[25] A. A. Langford, M. L. Fleet, B. P. Nelson, W. A. Lanford, and N. Maley, Phys. Rev. B **45**, 13 367 (1992).

[26] L. S. Sidhu, T. Kosteski, S. Zukotynski, and N. P. Kherani, J. Appl. Phys. **85**, 2574 (1999).

[27] D. Jousse, E. Bustarret, and F. Boulitrop, Solid State Commun. **55**, 435 (1985).

[28] A. H. Mahan, P. Rabiosson, and R. Tsu, Appl. Phys. Lett. **50**, 335 (1987).
[29] H. R. Shanks, F. R. Jeffrey, and M. E. Lowry, J. Phys. (Paris), Colloq. **42**, C4-773 (1981).
[30] D. Quicker and J. Kakalios, Phys. Rev. B **60**, 2449 (1999).
[31] S. Guha, J. Yang, D. L. Williamson, Y. Lubianiker, J. D. Cohen, and A. H. Mahan, Appl. Phys. Lett. **74**, 1860 (1999).
[32] V. F. Sears, Neutron News **3**, 26 (1992).
[33] L. A. Feigin and D. I. Svergun, *Structure Analysis by Small-Angle X-ray and Neutron Scattering* (Plenum, New York, 1987), p. 115.
[34] P. Debye, H. R. Anderson, and H. Brumberger, J. Appl. Phys. **28**, 679 (1957).
[35] S. Acco, D. L. Williamson, P. A. Stolk, F. W. Saris, M. J. van den Boogaard, W. C. Sinke, W. F. van der Weg, S. Roorda, and P. C. Zalm, Phys. Rev. B **53**, 4415 (1996).
[36] D. L. Williamson, S. Roorda, M. Chicoine, R. Tabti, P. A. Stolk, S. Acco, and F. W. Saris, Appl. Phys. Lett. **67**, 226 (1995).
[37] R. L. Mills, D. H. Liebenberg, J. C. Bronson, and L. C. Schmidt, J. Chem. Phys. **66**, 3076 (1977). The assumed density of D_2 is twice that of H_2 for same pressure.
[38] M. Roth, J. Appl. Crystallogr. **10**, 172 (1977).
[39] J. Ebothe, P. Roca i Cabarrocas, C. Godet, and B. Equer, Mater. Sci. Eng., B **42**, 105 (1996).
[40] D. M. Tanenbaum, A. L. Laracuente, and A. Gallagher, Phys. Rev. B **56**, 4243 (1997).
[41] R. W. Collins and H. Fujiwara, Curr. Opin. Solid State Mater. Sci. **2**, 417 (1997).
[42] M. C. M. van de Sanden, A. H. M. Smets, and W. M. M. Kessels, in *Amorphous and Heterogeneous Silicon-Based Films-2002*, edited by J. R. Abelson, J. B. Boyce, J. D. Cohen, H. Matsumura, and J. Robertson, MRS Symposia Proceedings No. 715 (Materials Research Society, Pittsburgh, 2002), p. A15.1.
[43] H. Pilsl, H. Hoffman, S. Hoffman, J. Kalus, A. W. Kencono, P. Lindner, and W. Ulbricht, J. Phys. Chem. **97**, 2745 (1993).
[44] J. E. Gerbi, P. Voyles, J. M. Gibson, and J. R. Abelson, in *Amorphous and Microcrystalline Silicon Technology-1998*, edited by R. Schropp, H. M. Branz, M. Hack, I. Shimizu, and S. Wagner, MRS Symposia Proceedings No. 507 (Materials Research Society, Pittsburgh, 1998), p. 429.
[45] F. Diehl, B. Schroeder, and H. Oechsner, J. Non-Cryst. Solids **227–230**, 973 (1998).
[46] Y. Lubianiker, J. D. Cohen, H.-C. Jin, and J. R. Abelson, Phys. Rev. B **60**, 4434 (1999).
[47] D. Kwon, C.-C. Chen, J. D. Cohen, H.-C. Jin, E. Hollar, I. Robertson, and J. R. Abelson, Phys. Rev. B **60**, 4442 (1999).
[48] M. Birkholz, B. Selle, W. Fuhs, and D. L. Williamson, in *Amorphous and Heterogeneous Silicon-Based Films-2001* (Ref. 9), p. A15.4.
[49] M. Luysberg, P. Hapke, R. Carius, and F. Finger, Philos. Mag. A **75**, 31 (1997).
[50] K. K. Gleason, M. A. Petrich, and J. A. Reimer, Phys. Rev. B **36**, 3259 (1987).
[51] J. A. Reimer, R. W. Vaughan, and J. C. Knights, Phys. Rev. Lett. **44**, 193 (1980).